High-Sensitivity Early Detection Biomedical Sensor for Tuberculosis With Low Losses in the Terahertz Regime Based on Photonic Crystal Fiber Technology

Nazmi A. MOHAMMED[1], Omar E. KHEDR[2,3*], El-Sayed M. EL-RABAIE[3], and Ashraf A. M. KHALAF[4]

[1]*Department of Electronics and Communication Engineering, Medina Higher Institute for Engineering and Technology, Giza 12947, Egypt*

[2]*Department of Communications and Electronics, Alexandria Higher Institute for Engineering and Technology, Alexandria 21311, Egypt*

[3]*Department of Electronics and Communications Engineering, Faculty of Electronic Engineering, Menoufia University, Menouf 32952, Egypt*

[4]*Department of Communications and Electronics, Faculty of Engineering, Minia University, Minia 61111, Egypt*

[*]Corresponding author: Omar E. KHEDR E-mail: omar.khedr@aiet.edu.eg

Abstract: Tuberculosis is one of the most contagious and lethal illnesses in the world, according to the World Health Organization. Tuberculosis had the leading mortality rate as a result of a single infection, ranking above HIV/AIDS. Early detection is an essential factor in patient treatment and can improve the survival rate. Detection methods should have high mobility, high accuracy, fast detection, and low losses. This work presents a novel biomedical photonic crystal fiber sensor, which can accurately detect and distinguish between the different types of tuberculosis bacteria. The designed sensor detects these types with high relative sensitivity and negligible losses compared to other photonic crystal fiber-based biomedical sensors. The proposed sensor exhibits a relative sensitivity of 90.6%, an effective area of $4.342\times10^{-8}\,\mathrm{m}^2$, with a negligible confinement loss of $3.13\times10^{-9}\,\mathrm{cm}^{-1}$, a remarkably low effective material loss of $0.0132\,\mathrm{cm}^{-1}$, and a numerical aperture of 0.3462. The proposed sensor is capable of operating in the terahertz regimes over a wide range (1 THz – 2.4 THz). An abbreviated review of non-optical detection techniques is also presented. An in-depth comparison between this work and recent related photonic crystal fiber-based literature is drawn to validate the efficacy and authenticity of the proposed design.

Keywords: Tuberculosis; photonic crystal fiber; relative sensitivity; terahertz; confinement loss; effective area

Citation: Nazmi A. MOHAMMED, Omar E. KHEDR, El-Sayed M. EL-RABAIE, and Ashraf A. M. KHALAF, "High-Sensitivity Early Detection Biomedical Sensor for Tuberculosis With Low Losses in the Terahertz Regime Based on Photonic Crystal Fiber Technology," *Photonic Sensors*, 2023, 13(2): 230202.

1. Introduction

Photonic crystals (PhCs) have become an attractive choice for optical data processing (ODP) applications. In recent years, they have been ranked among the most important platforms used in ODP applications and for making them cost-effective [1]. PhCs, in this type of application, are compared to famous photonic-based technologies, such as visible light communications (VLC) [2–8], semiconductor

Received: 8 July 2022 / Revised: 28 October 2022

DOI: 10.1007/s13320-023-0675-z
Article type: Regular

optical amplifiers (SOAs) [9], fiber Bragg grating (FBG) [10–12], Mach-Zehnder interferometer (MZI) [13, 14], free-space optical communication (FSO) [15, 16], and modulators used in optical networks [17]. Characteristics obtained from the photonic domain, including immunity to electromagnetic interference, safety in highly combustible environment, fast response speed, and long-range monitoring, are features that make PhC promising [18, 19]. Additional merits are low power consumption, flexibility in structural design, and excellent sensitivity measurement [20]. As a result, today, PhCs are frequently utilized in several ODP technologies, such as resonators [21], couplers [22], channel drop filters [23], optical modulators [24], oscillators [25], switches [26], logic gates [27], adders [28], subtractors [29], encoders [30], and sensors.

Recently, PhCs-based sensors have been considered among the most promising photonic-based sensing techniques. Their exceptional physical properties, such as reflectance/transmittance and increased sensitivity, are important factors for future sensing methods [31, 32]. In the last decade, PhCs have been used to provide accurate, real-time, and cost-effective photonic-based sensors [33–35].

Photonic crystal fibers (PCFs) are direct applications that utilize the advantages of PhCs in optical fibers. Due to their various capabilities, PCFs are getting tremendous attention from scientists in the field of optics. The primary aspect of PCFs, as optical waveguides, is the revolutionary methodology that they used for light propagation [36–38]. PCFs are preferable to alternative optical channels because of their durability, compact size, high tensile strength, and inexpensive cost [36, 39]. Also, design flexibility, single-mode propagation, high confinement, propagation in air and solid core, and controllable birefringence are extra advantages of PCFs [40, 41]. In addition to providing electromagnetic signal propagation interactions with liquids and gases, PCFs can be used in many sensing applications. Several PCF types have been designed and manufactured for that purpose, such as chemical sensors [42], temperature sensors [43], pressure sensors [44], salinity sensors [45], and blood component sensors [46].

In recent decades, scientists paid a lot of attention to the terahertz radiation band [47, 48]. Terahertz emission can be transmitted across optical fibers and poses no threat to human health [36]. Therefore, optical fiber-based sensors that operate in terahertz frequencies have been proposed and used in different real-life activities. Based on the aforementioned merits of PCFs, a wide range of PCF-based biomedical sensors were designed, tested, and sometimes fabricated. Some examples are blood component sensor [46], glucose concentration sensor [49], malaria detection sensor [50], protein detection [51], and sensors for different types of cancers [52, 53]. The most important PCF-sensing features (sometimes referred to as performance evaluation parameters) include relative sensitivity (RS), confinement loss (CL), effective material loss (EML), operating speed frequency, effective area (A_{eff}), numerical aperture (NA), and fabrication possibility using currently available technologies [54–56].

According to the worldwide tuberculosis report issued by the World Health Organization (WHO) in 2021, every year, 10 million people become infected with tuberculosis (TB) [57]. Despite the fact that tuberculosis is a preventable and curable disease, 1.5 million people die from it each year, making it the world's leading infectious killer [57]. TB is the greatest cause of death among human immunodeficiency virus (HIV) patients, as well as a significant contributor to antibiotic-resistant bacteria. TB is a contagious disease that is the primary cause of illness and death globally. TB was the top infectious agent-related cause of mortality, surpassing Acquired Immunodeficiency Syndrome HIV/AIDS [57]. In 2019, the most recent year during which the WHO published worldwide death estimates by cause, TB was the 13th largest cause of

death worldwide and the leading infectious agent-related cause of death [57]. In its last issued report on TB, the WHO predicted that in 2020, the disease was going to be the second biggest infectious agent-related cause of death [57]. It also estimated that in 2020, ten million people would have been infected with the TB [57]. There are 5.6 million men, 3.3 million women, and 1.1 million children diagnosed with TB around the world [57]. In this same report, it was expected that, in 2020, the number of fatalities of TB would increase, and previous declines in the annual number of tuberculosis cases would be slow down dramatically [57]. There were fewer TB diagnoses and treatments, as well as TB preventive treatment, in 2019 than in 2018 [57]. Modeling forecasts indicate that the disruptions induced by the pandemic could have a significantly greater impact on the number of persons contracting tuberculosis and dying from the disease in 2022. In conclusion, continuous and serious efforts should be done to design, test, and, if possible, fabricate then deliver to the medical field several devices, sensors, and machines that deal with such impairments. Furthermore, if these efforts are dedicated to meet early detection mechanisms, the outcomes would be attractive and useful. Early detection techniques must satisfy several requirements. Examples are high sensing accuracy, low operating losses, low power consumption, compact devices, and high response speeds.

This work presents a serious attempt to meet the majority of the aforementioned requirements. A PCF sensor proposed is designed, simulated, and evaluated. Key performance evaluation parameters, such as RS, CL, EML, A_{eff}, and NA, are also addressed. A comparison with related PCF-based techniques is achieved to confirm the novelty of the proposed design.

The remainder of this article is organized as follows: the sensor structure design is presented in Section 2. Section 3 discusses the performance evaluation parameters of the proposed sensor. The results, specifications, and sensing characteristics of the new design are presented in Section 4. Verification of this work's sensing capabilities is proven through an in-depth comparison with related photonic biomedical sensors in Section 5. Finally, a conclusion that includes the value of the proposed sensor's performance and characteristics is drawn in Section 6.

2. Sensor structure design

The cross-sectional structure of the proposed PCF sensor is introduced in Fig. 1. Teflon, zeonex, silica, and topas are the most popular materials utilized as the background for terahertz-based PCFs, due to their excellent characteristics and lower absorption loss compared to other optical material sensors [36]. Zeonex has a minimum absorption loss of 0.2 cm^{-1}, limited water absorption, high transparency, increased glass transition temperature, and excellent optical stability following exposure to humidity and heat. Hence, it is chosen as the sensor's background material [58, 59].

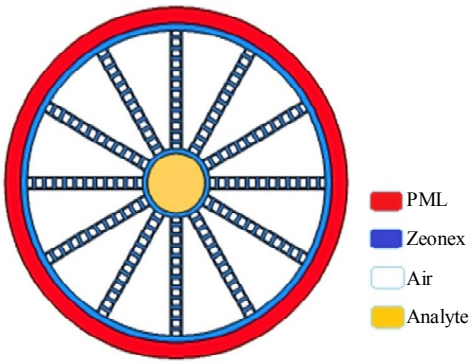

Fig. 1 Cross-sectional view of the proposed tuberculosis sensor.

A detailed view of the proposed sensor's structure, including geometrical parameters, is shown in Fig. 2. This detailed cross-sectional view shows that a single circular air hole with a radius (X) is drilled into the core, which will contain the sample of analyte cells. The cladding region starts from the inner circle with a radius C_1, which measures 100 µm and ends with the outer circle radius (C_2), which measures 440 µm. The thickness of the clad's outer

circle (t) is equal to 20 μm. The cladding region consists of twelve symmetric syllables of air holes placed in the cladding section. It also has 12 strips of length (L) which contain 12 similar rectangular air holes. The width of the strip is denoted by (W_1) and is equal to 35 μm. The rectangular air hole inside the strip has a width of W_2 and a length of W_3, with values of 20 μm and 25 μm, respectively. The distance between each rectangular air hole is denoted by W_4 and is equal to 10 μm.

Finally, the rectangular air holes are located at the center of the strip at a distance of 5 μm from the wall of the strip. At the outer area of the presented sensor, a perfectly matched layer (PML) boundary condition is used. Its major role is to absorb the light signal escaping from the core and traveling towards the cladding, preventing reflection back towards the core. Its radius is 10% of the outermost circle of the cladding region. Geometrical parameters are summarized in Table 1.

Table 1 Geometrical parameters values of the proposed sensor.

Parameter	Description	Value (μm)
X	Core radius	85
C_1	Clad's inner radius	100
C_2	Clad's outer radius	440
t	Clad's outer circle thickness	20
L	Length of the strip	340
W_1	Width of the strip	35
W_2	Width of the rectangular air hole	20
W_3	Length of the rectangular air hole	25
W_4	Distance between rectangular air hole and each other	10
W_5	Distance between the rectangular air hole and the wall	5

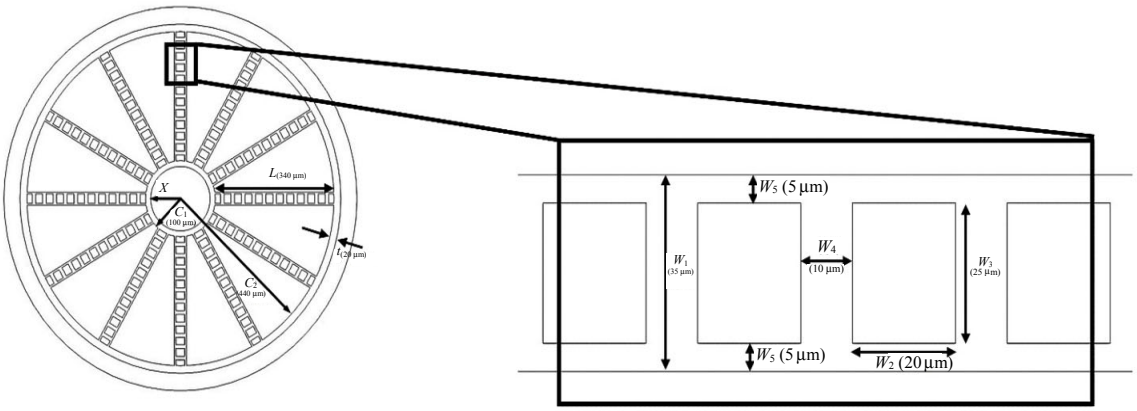

Fig. 2 Geometrical parameters of the proposed sensor.

Nowadays, numerous fiber fabrication techniques, which are used to manufacture PCF sensors, are commercially available, such as sol-gel [60], capillary stacking [61], stack and draw [62], 3D printing [63], and extrusion [64]. Since the proposed sensor PCF includes square and rectangular air holes, the 3D (3-dimensional)-printing method is the best option for fabrication. The 3D printing method has been effectively utilized to fabricate symmetries structures. In recent years, the Max Planck Institute has manufactured a variety of complex-shaped PCF sensors [65]. However, the proposed structure may require an accurate fabrication procedure. The proposed sensor structure was designed and simulated using the COMSOL Multiphysics software (version 5.6). Its optical properties were analyzed by using the finite element method (FEM). This method is more accurate than other well-known numerical approaches [66]. The meshing process was performed using in a finer mesh, with a total of 22 130 domains and 3 472 boundary elements, as shown in Fig. 3.

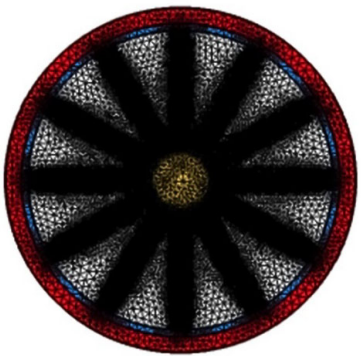

Fig. 3 Finer mesh of the proposed sensor.

3. Performance evaluation parameters

To evaluate the effectiveness of detection of the proposed PCF sensor, as well as its ability to meet the early detection requirements previously indicated, different evaluation parameters should be used to analyze the sensor's performance. For biomedical sensing applications, relative sensitivity (RS), confinement loss (CL), effective material loss (EML), operating speed frequency, effective area (A_{eff}), and numerical aperture (NA) are considered as the characteristic parameters. The efficiency of a biomedical sensor is determined by these features. For PCF-based sensors, the light must propagate mainly in the core region and be heavily confined to the core.

The CL property is utilized to determine light's confinement in the core region. It represents the light that passes from the core to the cladding region due to the finite number of air holes. Equation (1) is utilized in the calculation of CL [56,67]:

$$\text{CL} = \left(\frac{4\pi f}{c}\right) \times \text{Im}\left(n_{\text{eff}}\right) \quad (\text{cm}^{-1}) \qquad (1)$$

where f represents the resonant frequency, c represents the velocity of light, and Im(n_{eff}) represents the effective refractive index's imaginary value.

EML is the quantity of energy absorbed per unit length by the background material. Loss of the molecules of the material will contribute to the dissipation of some optical power, such as heat. EML should be minimal, if the PCF model is properly constructed, and the area of the background material is as small as possible. Equation (2) is used to calculate EML [56, 67]:

$$\text{EML} = \left(\frac{\sqrt{\dfrac{\varepsilon_0}{\mu_0}} \displaystyle\int_{\text{mat}} n_{\text{mat}} \left|\mathbf{E}\right|^2 \alpha_{\text{mat}} \text{d}A}{\displaystyle\int_{\text{all}} 0.5\left(\mathbf{E}\times\mathbf{H}\right)\hat{\mathbf{z}}\text{d}A} \right) \quad (\text{cm}^{-1}) \quad (2)$$

where **H** represents the intensity of the magnetic field in the z-direction, **E** represents the intensity of the electric field in the z-direction, and ε_0 and μ_0 represent the permittivity and permeability of free space, respectively. The background material refractive index is denoted as (n_{mat}), and α_{mat} represents the absorption loss of the substance.

A_{eff} is another important feature. The electric field distribution (E) must be inserted into the core for the single-mode propagation. Any PCF-based sensor's effective area measures its significant detecting region. A_{eff} is determined by (3) [56, 67]

$$A_{\text{eff}} = \frac{\left(\iint \left|E\right|^2 \text{d}x\text{d}y\right)^2}{\left(\iint \left|E\right|^4 \text{d}x\text{d}y\right)} \quad (\mu\text{m}^2). \qquad (3)$$

NA represents the variety of incident light angles that the fiber transmits and receives. NA is a unitless value that depends on light velocity (c), effective area A_{eff}, and frequency (f). For sensing applications, a greater NA is recommended, which can be obtained by decreasing A_{eff}. The value of NA is determined by (4) [56, 68]:

$$\text{NA} = \frac{1}{\sqrt{1 + \dfrac{\pi f^2 \left(A_{\text{eff}}\right)}{c^2}}}. \qquad (4)$$

RS is the primary optical characteristic that effectively addresses sensing capability. The percentage of RS estimates the power that passes through the core relative to the total power inserted. Equation (5) is utilized to determine the value of RS [56, 68]:

$$\text{RS} = \left[\left(\frac{\displaystyle\int_{\text{sample}} \text{Re}\left(H_y E_x - H_x E_y\right) \text{d}x\text{d}y}{\displaystyle\int_{\text{all}} \text{Re}\left(H_y E_x - H_x E_y\right) \text{d}x\text{d}y} \right) \frac{n_r}{n_{\text{eff}}} \right] * 100\% \qquad (5)$$

where n_r represents the refractive index of the tuberculosis infected samples, and n_{eff} is the real component of the effective refractive index. E_x and E_y represent the electric fields in x and y polarizations, respectively. H_x and H_y represent the magnetic fields in x and y polarizations, respectively.

4. Results and discussion

It is important to state that the design stages of the sensor will mainly depend on the accuracy measurement of the refractive index (RI) of normal cells and those infected with several types of mycobacterium tuberculosis. RIs of normal and several samples infected with different types of mycobacterium tuberculosis are shown in Table 2, which will be used to indicate the sample's status [69–71]. Each precise refractive index measurement will be associated with a particular type of normal or infected sample, as shown in Table 2.

Table 2 RIs of cells infected with several types of tuberculosis.

Tuberculosis samples		RI
Normal blood plasma (NPS)		1.351
Cells infected with several types of tuberculosis	TB1	1.343
	TB2	1.345
	TB3	1.347
	TB4	1.348

Several optimization techniques and trial methods are usually applied to the PhC/PCF-based sensor designs to find the optimum values for the operating characteristics or evaluation parameters. Examples are adjusting the radius of the holes [35, 72], examining various values of the cavity's radius [30], varying the background material [73], setting different distances for the displacement between the main cavity/cavities and the origin of the lattice [74, 75], and varying the core radius [36].

This work will assume that adjusting the radius of the core is the main optimization parameter (i.e., others optimization parameters are tested, but this is the one chosen). This is done for several reasons. The first is that a large number of tissue cells is required for accurate sensing. Secondly, an optimization of all evaluation parameters (i.e., EML, CL, operating speed frequency, A_{eff}, NA, and RS) is required for every tissue cell tested. Finally, it will be shown that the outcome of these intensive optimization process/trial methods will be utilized to find the optimum value for the radius that will lead to the best performance evaluation parameters. All numerical analyses are calculated for a frequency range of 1.0 THz to 2.4 THz and are computed with COMSOL Multiphysics (version 5.6). The performance of each of the evaluation parameters will be presented separately in the following sub-sections.

4.1 Effective material loss (EML)

Figure 4 illustrates the EML of the proposed sensor for detecting different tuberculosis-infected samples, as a function of the frequency range from 1 THz to 2.4 THz. EML can be calculated from (2), as indicated in Section 3. EML versus frequency shows that EML starts to decrease from 1 THz to 2 THz for all samples. From 2 THz to 2.2 THz, EML is nearly constant. After 2.2 THz, EML starts to slightly increase once more for all tuberculosis-infected samples. This means that 2.2 THz is the optimum frequency for operation, in respect to EML, for all samples. Meanwhile, Fig. 5 shows the variation of EML with respect to variations in a core radius (X), in order to find the optimum X. X will vary from 85μm to 125 μm. This clearly shows that the minimum EML occurs at X of 115 μm, making this the optimum value.

The numerical values at an X of 115 μm and a frequency of 2.2 THz for EML are found to be as follows: 0.013 286 for normal blood plasma, and 0.014 019, 0.013 831, 0.013 647, and 0.013 556 for samples infected with different tuberculosis bacteria, i.e., TB1, TB2, TB3, and TB4, respectively.

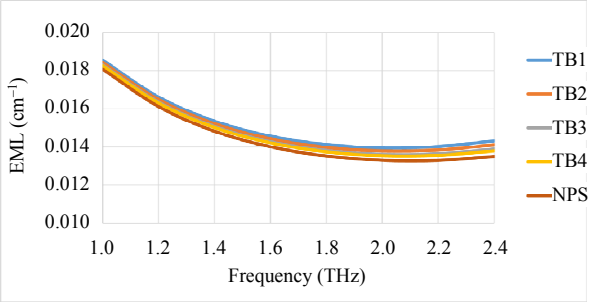

Fig. 4 EML of the proposed sensor for various samples infected with tuberculosis versus frequency.

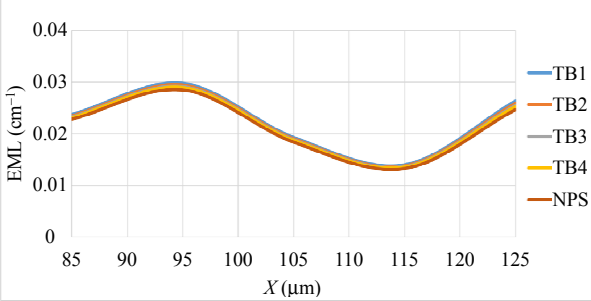

Fig. 5 EML of the proposed sensor for various samples infected with tuberculosis versus X at 2.2 THz.

4.2 Relative sensitivity (RS)

Figure 6 illustrates the variation of RS within the frequency range from 1 THz to 2.4 THz, for various tissue samples infected with tuberculosis. As previously indicated, (5) provides the formula for calculating RS. RS starts to increase from 1 THz to 1.8 THz, for all tissues samples. From 1.8 THz to 2.4 THz, it is almost constant for all infected samples. Since RS is constant for frequencies higher than 1.8 THz, 2.2 THz is chosen to be the optimum frequency for all tissue samples, regarding this parameter.

On the other hand, Fig. 7 illustrates the variation in RS relative to X. This is performed in order to find the best value for X, which will achieve the optimum value for RS. X will vary from 85 μm to 125 μm. Its optimum value is found to be 115 μm. For X values higher or lower than 115 μm, the values of RS are less than expected.

For an X of 115 μm and a frequency of 2.2 THz, RS values are found to be as follows: 90.6% for normal blood plasma and 89.9%, 90.1%, 90.2%, and 90.3% for samples infected with different types of tuberculosis, i.e., TB1, TB2, TB3, and TB4, respectively.

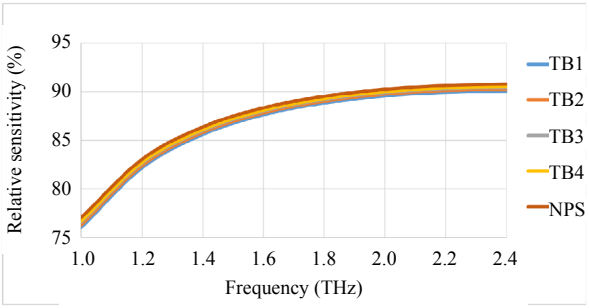

Fig. 6 RS of the proposed sensor for various samples infected with tuberculosis versus frequency.

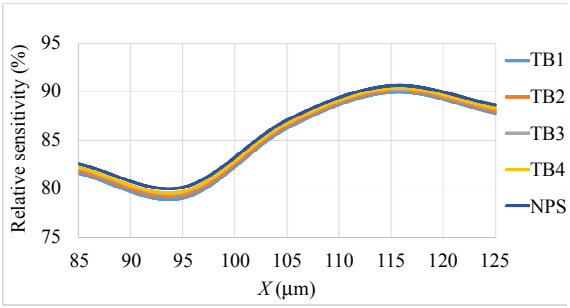

Fig. 7 RS of the proposed sensor for various tuberculosis-infected samples versus X at 2.2 THz.

4.3 Effective area (A_{eff})

A_{eff} versus frequency of the suggested tuberculosis sensor is shown in Fig. 8. This graphical representation shows that A_{eff} decreases with increments in frequency within the range of 1 THz to 2.4 THz, for all samples infected with tuberculosis. Despite that the 2.4 THz is the optimum value for the effective area, the change in A_{eff} between 2.2 THz to 2.4 THz is very small and can be neglected. The change is nearly about 0.15×10^{-8} m^2. So, for the continuity of the superior advantages in both relative sensitivity and effective material loss at 2.2 THz. The frequency of 2.2 THz is still remaining the optimum operating frequency for the proposed sensor.

Figure 9 presents the variation in A_{eff} relative to X. The graphical representation shows an increase in A_{eff}, as X increases from 85 μm to 115 μm. From 115 μm to 125 μm, A_{eff} for all tuberculosis-infected samples slightly decreases by 0.1×10^{-8}m^2, which brings X to

115 μm, the optimum radius for the proposed design.

The numerical values for A_{eff} at X of 115 μm and a frequency of 2.2 THz are found to be as follows: 4.35×10^{-8} m^2 for normal blood plasma, and 4.34×10^{-8} m^2, 4.342×10^{-8} m^2, 4.343×10^{-8} m^2, and $4.344\times m^2$ for infected samples of different types of tuberculosis, i.e., TB1, TB2, TB3, and TB4, respectively.

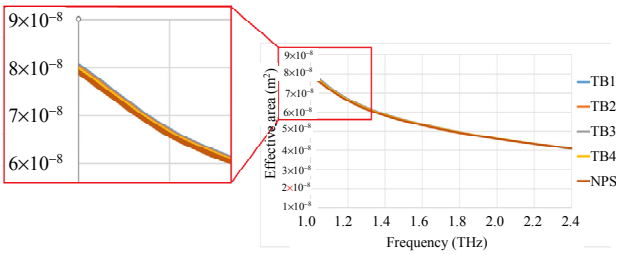

Fig. 8 A_{eff} of the proposed sensor for various tuberculosis-infected samples versus frequency.

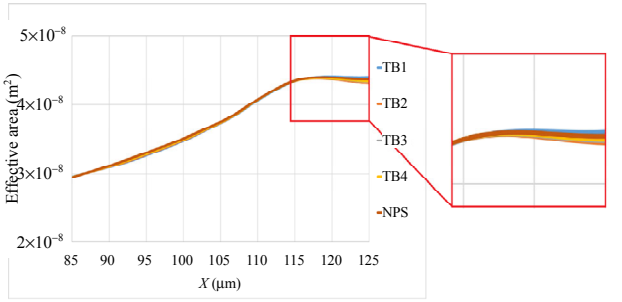

Fig. 9 A_{eff} of the proposed sensor for various tuberculosis-infected samples versus X at 2.2 THz.

4.4 Confinement loss (CL)

Figure 10 presents the variation in CL versus frequency. It can be seen that CL decreases as frequency increases for all tuberculosis-infected samples from 1 THz to 2.4 THz. Thus, the linearity behavior is obvious for all samples, within this frequency range. However, a non-linearity behavior occurs after 2.4 THz. Despite this issue, the minimum CL for all tuberculosis-infected samples is found to occur at 2.4 THz. As such, 2.2 THz is chosen as the optimum frequency for the proposed sensor, for three reasons. The first reason is to ensure that the frequency will be within the linear region of CL. The second reason is to ensure the continuity of the superior values for both RS, EML, and A_{eff}, which occur at 2.2 THz. The third reason is that the variation in the values of CL for all tuberculosis-infected samples between 2.2 THz and 2.4 THz is nearly around 10^{-1} or less, which can be neglected to ensure the aforementioned advantages.

The feature of CL versus frequency has been examined at different X starting from 85μm to 125 μm, same as RS, EML, and A_{eff}. Figure 11 illustrates the variation of CL for X from 85μm to 125 μm, at a frequency of 2.2 THz. CL sees its minimum value for all tuberculosis-infected samples at an X of 115 μm. This makes the value of 115 μm for X optimum for most of the evaluation parameters.

The numerical values for CL, at an X of 115 μm and a frequency of 2.2 THz, are found to be as follows: 3.13×10^{-9} for normal blood plasma and 4.83×10^{-9}, 4.34×10^{-9}, 3.89×10^{-9}, and 3.68×10^{-9} for samples infected with different types of tuberculosis, i.e., TB1, TB2, TB3, and TB4, respectively.

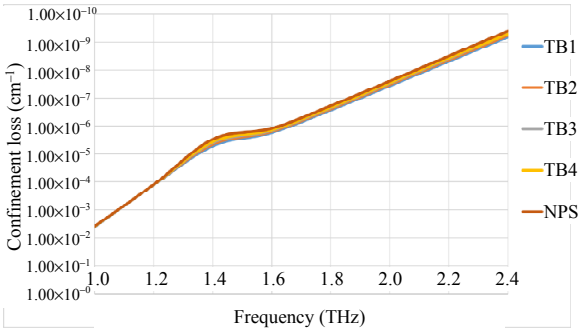

Fig. 10 CL of the proposed sensor for various tuberculosis-infected samples versus frequency.

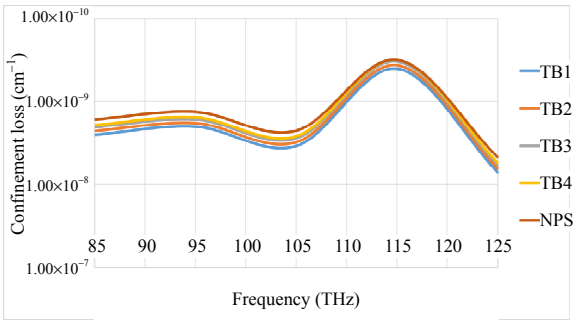

Fig. 11 CL of the proposed sensor for various tuberculosis-infected samples versus X at 2.2 THz.

4.5 Numerical aperture (NA)

NA is another essential photonic characteristic that mainly depends on A_{eff} and frequency. NA reflects the ability of the fiber to keep light and other

waves confined within it without dispersion. To attain a high numerical value for NA, the RI of the core must be greater than that of the cladding.

Figure 12 presents the relationship between NA and the operating frequency of various tuberculosis-infected samples. NA is reduced, as frequency increases because it is inversely proportional to it. NA should be as high as possible (i.e., up to a certain limit, to permit single-mode operation only). So, in order to maintain single-mode operation, the allowable range for NA should be from 1.4 THz to 2.4 THz. Since there is no significant difference between 2.2 THz and 2.4 THz, the optimum operation frequency is chosen to be 2.2 THz, due to the aforementioned advantages gained at 2.2 THz.

On the other hand, Fig. 13 represents the variation in NA versus X in various tuberculosis-infected samples. It clearly shows that NA decreases as X increases. The slight change in NA between an X of 85 µm and 115 µm is negligeable. Thus, for the sake of the previously stated benefits related to evaluation parameters (i.e., RS, EML, CL, and A_{eff}) at an X of 115 µm, this value is chosen as the optimum X.

The numerical values for NA, at an X of 115 µm and a frequency of 2.2 THz, are found to be as follows: 0.346 2 for normal blood plasma and 0.346 4, 0.346 3, 0.346 3, and 0.346 2 for samples infected with different types of tuberculosis, i.e., TB1, TB2, TB3, and TB4, respectively. Figure 14 represents the electric field distribution for various tuberculosis-infected samples, at the optimum frequency of 2.2 THz and the optimum X of 115 µm.

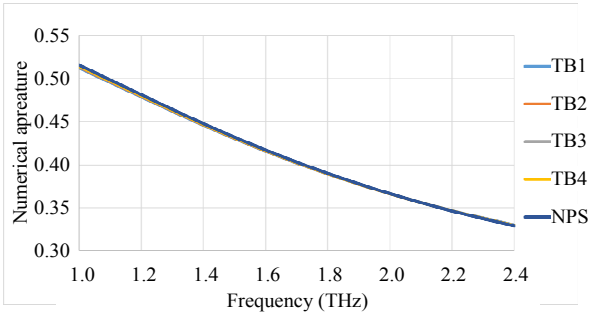

Fig. 12 NA of the proposed sensor for various tuberculosis-infected samples versus frequency.

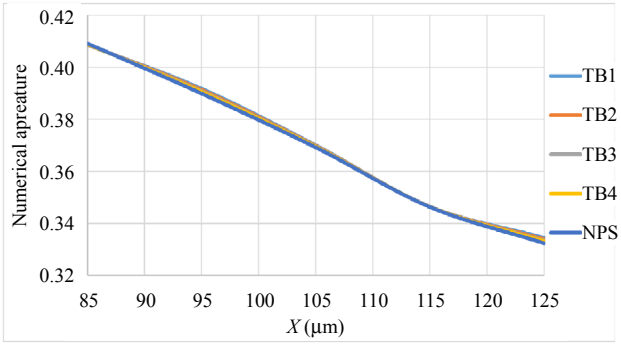

Fig. 13 NA of the proposed sensor for various tuberculosis-infected samples versus X at 2.2 THz.

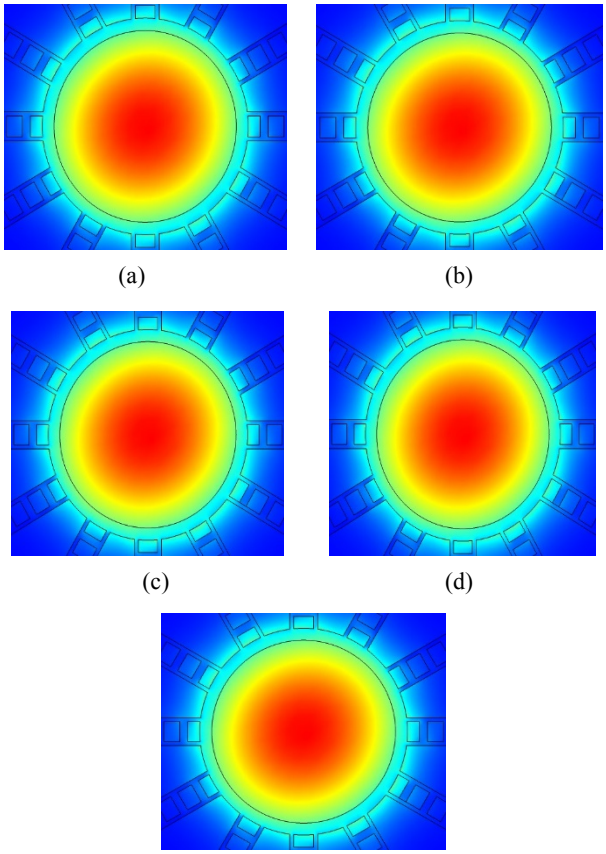

Fig. 14 Distribution of the electric field for different brain tissue samples at 2.2 THz: (a) NPS, n_{eff}=1.310 8; (b) TB1, n_{eff} =1.312 5; (c) TB2, n_{eff}=1.314 3; (d) TB3, n_{eff}=1.315 2; (e) TB4, n_{eff}=1.317 9.

5. Comparison with related literature and non-optical detection techniques

5.1 Non-optical detection techniques

The goal of this section is to review the famous commercial detection techniques for the different tuberculosis samples with their advantages, disadvantages, and cost. This should provide an

insight view of the promising features of the proposed design, especially when merged with the following sub-section (i.e., 5.2).

Traditional tuberculosis tests are either inaccurate or take too long to complete [76, 77]. Additionally, a rapid and reliable diagnostic approach that distinguishes between active and latent tuberculosis infections is absent. The current standard diagnostic tests for tuberculosis are as follows: the chest x-ray examination (CXR), tuberculin skin test (TST), and blood test "interferon-gamma release assays (IGRAs)". All have their limitations, such as a chest x-ray alone is inconclusive; the TST lacks specificity and reliability. These methods can be improved by merging with other techniques such as artificial intelligence [78, 79], it will considerably boost their capabilities. Table 3 shows a comparison between different non-optical techniques to detect tuberculosis with their merits, disadvantages, and cost.

Table 3 Non-optical detection techniques with a price range, advantages, and disadvantages [80–83].

Technique	Advantages	Disadvantages	Price
The chest x-rays (CXR)	(1) Reduced operating expenses (2) Enhanced image quality with the ability to enlarge (3) Reduced dose of radiation (4) Enhanced portable systems suitable for use with mobile units (5) The possibility of computer-aided detection, without human interference (6) Enhanced (digital) archiving ability (7) The capability of transmitting images online	(1) It generates 2-dimentional (2D) images of 3D systems (2) There is a reader-to-reader modification (3) The specificity is low, because no abnormality is conclusive of tuberculosis (4) There is a total absence of a universally accepted reporting system (5) Ionizing radiation is used to detect diseases (6) There is a requirement for specialized equipment (with an adequate input power supply) (7) The machine must be operated and the results interpreted by qualified staff (8) Limited access in rural areas (9) There is only a limited amount of hard copy archiving	8$ USD [84]
Tuberculin skin test (TST)	(1) Inexpensive (2) Used for over a century with lots of experience (3) Individuals with the following medical problems are preferred in this test: diabetes mellitus, chronic renal failure (4) Easy to conduct	(1) Appropriate placement of the TST into the skin requires skilled staff (2) After a 48- to 72-hour incubation period, a second clinic visit is required (3) Since inter-reader and intra-reader fluctuation is common, a skilled technician is required to read and interpret the TST result (4) Sensitivity is reduced, particularly in people with compromised immune systems (5) A positive TST result does not necessarily indicate the presence of the mycobacterium tuberculosis bacteria in the body at the time of testing	3$–13$ USD [85]
Blood test (interferon-gamma release assays, IGRAs)	(1) Achieves greater sensitivity and specificity (2) Only one clinic consultation is required (3) Can provide results in less than 24 hours; (4) Relies on an immunological response based on relatively short-lived T-effector cells; (5) A positive result implies that the immune system has recently been exposed to the M TB bacteria	(1) The test should be performed by a qualified operator in a laboratory environment (2) High cost (3) More laboratory resources required (4) Depends on the complicated process of lymphocyte separation (5) Lack of prospective studies	35$–40$ USD [85]

5.2 Comparison with related literature

This section will present an in-depth comparison between this work and other studies that explores different types of biosensors, using PCF techniques. Before starting, it should be mentioned that there is a serious shortage in the field of sensing and identifying samples infected with different types of tuberculosis, as well as normal uninfected samples, using photonics-based sensing techniques, especially PCFs.

Table 4 presents a comparison between the literature related to PCF-based biosensors and this

work. This research demonstrates the novelty of introducing a biomedical sensor, with attractive features, which can detect different types of tuberculosis bacteria, using a PCF platform. The most promising feature in the proposed design is its RS. The design proposed in this work provides a 90.6% RS, which is considered as a key feature. The ultra-high-speed operation, which is an inherent characteristic of all photonic-based sensing techniques (as indicated in Section 4), especially in PCF-based ones, is clear in this work. The widest possible operating frequency range (1 THz – 2.4 THz) is also achieved in this study. From this work's results and discussion, which can be seen in Section 4, 2.2 THz is found to be the optimum value for the accurate sensing operation. The use of zeonex, as the background material for this design, is an advantage, as it is in one other sensor, as seen in Table 4. The advantages of this material are previously covered in Section 2.

To ensure the smooth production of the proposed design, it is important to evaluate the impact of the fabrication tolerances. In the standard fabrication procedure, 2% tolerance is allowed in global parameters. Since the rectangular holes in the strip will be challenging to be fabricated using the current technology, it will be varied by ±2% and investigate its effect on the evaluation parameters. The performance of the proposed PCF sensor with ±2% variations shows that RS varies from 90.6% to 88.9% at its lowest value. However, CL varies by nearly around 10^{-1} below its value. EML varies from 0.013 2 in its original value to be 0.008 2. A_{eff} and NA are almost the same without any affect to the ±2% change in the rectangular holes in the strip.

Table 4 Comparison between the proposed tuberculosis sensor and biosensors based on photonic crystal fiber.

Ref.	Detection target	Operating frequency (THz)	Background material	A_{eff}	RS (%)	CL	EML (cm^{-1})	NA
[86] 2018	Cancers	–	Silica	–	–	209.12 dB/m	–	–
[87] 2019	Blood Components	1.5	Topas	1.55×10^{5} μm²	80.93	–	–	–
[88] 2021	Blood Components	1.0	Topas	1.86×10^{5} μm²	87.68	1.86×10^{-9} cm^{-1}	–	–
[89] 2020	Biosensor	1.0	Topas	–	82.26	5.84×10^{-8} dB/m	–	–
[90] 2021	Biosensor	0.8–3	Zeonex	1.32×10^{-7} m²	88.36	5.55×10^{-8} dB/m	0.006 99	–
[91] 2019	Biosensor	0.8–1.4	Topas	1.1×10^{-7} m²	–	5.42×10^{-13} dB/cm	0.066	0.518
[92] 2020	Biosensor	1	Zeonex	1.24×10^{5} μm²	87.02	1.95×10^{-3} cm^{-1}	0.009	–
[93] 2021	Biochemical	1–2	Zeonex	97 657 μm²	77.71	2.8×10^{-11} cm^{-1}	0.004 8	–
[94] 2020	Chemical	1.14	TOPAS	1.39×10^{5} μm²	70	10^{-11} cm^{-1}	–	0.557
[95] 2019	Blood components	–	Silica	–	66.46	$8.134\,3\times10^{-11}$ dB/cm	–	–
[68] 2017	Chemical	1.6	Silica	69 800 μm²	85.7	1.7×10^{-9} cm^{-1}	–	0.372
[96] 2018	Chemical	2.0	Zeonex	1.5×10^{5} μm²	85.80	1.62×10^{-9} cm^{-1}	0.023	–
This Work	Biosensor	1–2.4	Zeonex	4.342×10^{-8} m²	90.6	3.13×10^{-9} cm^{-1}	0.013 2	0.346 2

The proposed design has a remarkable performance in A_{eff}, which is found to be 4.342×10^{-8} m^2, the optimum value among all biosensors, as indicated in Table 4. This is a key factor when integrating this biosensor with other medical/diagnostic systems currently in use. Regarding the performance of the losses, the proposed design shows acceptable performance, with an EML of 0.013 2 cm^{-1}. While for CL, its performance was acceptable, with 3.13×10^{-9} cm^{-1}. Finally, for NA, preferred to be large without exceeding a certain limit (i.e., the limit that can hinder single-mode operation), the proposed design yields a suitable value of 0.3462.

6. Conclusions

Early detection techniques are among the most effective methods of reducing the growing number of tuberculosis infections. The key to improve survival rates is early diagnosis. This work introduces a novel PCF structure that successfully accomplishes the objectives of this goals. The proposed sensor is capable of accurately and simultaneously discriminating between normal blood plasma cells and those infected with four different types of tuberculosis bacteria. The proposed structure has been numerically evaluated. The simulation results demonstrate that the proposed sensor is effective in recognizing different types of tuberculosis bacteria. The proposed sensor exhibits the highest RS of 90.6%, an A_{eff} of 4.342×10^{-8} m^2, a negligible CL of 3.13×10^{-9} cm^{-1}, a remarkably low EML of 0.013 2 cm^{-1}, and finally, a suitable NA of 0.346 2. These levels are significant in comparison with other biosensors in the literature, in general. It is noteworthy to mention that the proposed sensor operates in the terahertz regime. A comparison is conducted with other biosensors in the literature, and the remarkable nature of the proposed sensor's performance indicators is demonstrated.

References

[1] N, A. Mohammed, O. E. Khedr, E. M. El-Rabaie, and A. A. M. Khalaf, "Brain tumors biomedical sensor with high-quality factor and ultra-compact size based on nanocavity 2D photonic crystal," *Alexandria Engineering Journal*, 2022 (https://doi.org/10.1016/j.aej.2022.09.020).

[2] N. A. Mohamed, A. M. Aly, A. K. AboulSeoud, and M. H. Aly, "Indoor wireless optical communication systems: effect of ambient noise," *Optical Engineering*, 2014, 53: 055109.

[3] K. A. Badawi, N. A. Mohammed, and M. H. Aly, "Exploring BER performance of a SC-LPPM based LOS-VLC system with distinctive lighting," *Journal of Optoelectronics and Advanced Materials*, 2018, 20(5–6): 290–301.

[4] N. A. Mohammed and K. A. Badawi, "Design and performance evaluation for a non-line of sight VLC dimmable system based on SC-LPPM," *IEEE Access*, 2018, 6: 52393–52405.

[5] N. A. Mohammed and M. A. Elkarim, "Exploring the effect of diffuse reflection on indoor localization systems based on RSSI-VLC," *Optics Express*, 2015, 23(16): 20297–20313.

[6] M. A. Elkarim, N. A. Mohammed, and M. H. Aly, "Exploring the performance of indoor localization systems based on VLC-RSSI, including the effect of NLOS components using two light-emitting diode lighting systems," *Optical Engineering*, 2015, 54(10): 105110.

[7] N. A. Mohammed, K. A. Badawi, A. A. M. Khalaf, and S. El-Rabaie, "Dimming control schemes combining IEEE 802.15.7 and SC-LPPM modulation schemes with an adaptive M-QAM OFDM for indoor LOS VLC systems," *Opto-Electronics Review*, 2020, 28: 203–212.

[8] N. A. Mohammed, M. M. Elnabawy, and A. A. M. Khalaf, "PAPR reduction using a combination between precoding andnon-linear companding techniques for ACO-OFDM-based VLC systems," *Opto-Electronics Review*, 2021, 29: 59–70.

[9] M. I. Shehata and N. A. Mohammed, "Design and optimization of novel two inputs optical logic gates (NOT, AND, OR, and NOR) based on single commercial TW-SOA operating at 40 Gbit/s," *Optical and Quantum Electronics*, 2016, 48(6): 1–16.

[10] N. A. Mohammed and H. O. El Serafy, "Ultra-sensitive quasi-ditributed temperature sensor based on an apodized fiber Bragg grating," *Applied Optics*, 2018, 57(2): 273–282.

[11] N. A. Mohammed, M. N. Okasha, and H. M. Aly, "A wideband apodized FBG dispersion compensator in long haul WDM systems," *Journal of Optoelectronics and Advanced Materials*, 2016, 18(5–6): 475–479.

[12] N. A. Mohammed and N. M. Okasha, "Single-and dual-band dispersion compensation unit using apodized chirped fiber Bragg grating," *Journal of Computational Electronics*, 2018, 17(1): 349–360.

[13] N. A. Mohammed, H. S. Abo Elnasr, and M. H. Aly, "Analysis and design of an electro-optic 2 × 2 switch using Ti: $KNbO_3$ as a waveguide based on MZI at 1.3 μm," *Optical and Quantum Electronics*, 2014, 46(2): 295–304.

[14] N. A. Mohammed, H. S. A. Elnasr, and M. H. Aly, "Performance evaluation and enhancement of 2×2 Ti: $LiNbO_3$ Mach-Zehnder interferometer switch at 1.3 μm and 1.55 μm," *The Open Electrical & Electronic Engineering Journal*, 2012, 6(1): 36–49.

[15] A. S. El-Wakeel, N. A. Mohammed, and M. H. Aly, "Free space optical communications system performance under atmospheric scattering and turbulence for 850 and 1550 nm operation," *Applied Optics*, 2016, 55(26): 7276–7286.

[16] N. A. Mohammed, M. R. Abaza, and M. H. Aly, "Improved performance of M-ary PPM in different free-space optical channels due to reed solomon code using APD," *International Journal of Scientific & Engineering Research*, 2011, 2(4): 82–85.

[17] N. A. Mohammed and A. H. Mansi, "Performance enhancement and capacity enlargement for a DWDM-PON system utilizing an optimized cross seeding rayleigh backscattering design," *Applied Sciences*, 2019, 9(21): 4520.

[18] Y. Zhang, Y. Zhao, and R. Lv, "A review for optical sensors based on photonic crystal cavities," *Sensors and Actuators A: Physical*, 2015, 233:374–389.

[19] Y. Zhang, Y. Zhao, T. Zhou, and Q. Wu, "Applications and developments of on-chip biochemical sensors based on optofluidic photonic crystal cavities," *Lab on a Chip*, 2018, 18(1): 57–74.

[20] W. S. Fegadolli, J. E. B. Oliveira, V. R. Almeida, and A. Scherer, "Compact and low power consumption tunable photonic crystal nanobeam cavity," *Optics Express*, 2013, 21(3): 3861–3871.

[21] F. Sun, B. Dong, J. Wei, Y. Ma, H. Tian, and C. Lee, "Demonstration of mid-infrared slow light one-dimensional photonic crystal ring resonator with high- order photonic bandgap," *Optics Express*, 2020, 28: 30736–30747.

[22] H. Sharifi, S. M. Hamidi, and K. Navi, "All-optical photonic crystal logic gates using nonlinear directional coupler," *Photonics and Nanostructures-Fundamentals and Applications*, 2017, 27: 55–63.

[23] J. Divya, S. Selvendran, and A. S. Raja, "Two-dimensional photonic crystal ring resonator-based channel drop filter for CWDM application," *Photonic Network Communications*, 2018, 35: 353–363.

[24] M. Li, J. Ling, Y. He, U. A. Javid, S. Xue, and Q. Lin, "Lithium niobate photonic-crystal electro-optic modulator," *Nature Communications*, 2020, 11(1): 1–8.

[25] G. Marty, S. Combrié, F. Raineri, and A. D. Rossi, "Photonic crystal optical parametric oscillator," *Nature Photonics*, 2021, 15(1): 53–58.

[26] R. Rajasekar, K. Parameshwari, and S. Robinson, "Nano-optical switch based on photonic crystal ring resonator," *Plasmonics*, 2019, 14(6): 1687–1697.

[27] T. S. Mostafa, N. A. Mohammed, and E. El-Rabaie, "Ultra-high bit rate all-optical AND/OR logic gates based on photonic crystal with multi-wavelength simultaneous operation," *Journal of Modern Optics*, 2019, 66: 1005–1016.

[28] M. M. Karkhanehchi, F. Parandin, and A. Zahedi, "Design of an all optical half-adder based on 2D photonic crystals," *Photonic Network Communications*, 2017, 33: 159–165.

[29] F. Parandin, R. Kamarian, and M. Jomour, "A novel design of all optical half-subtractor using a square lattice photonic crystals," *Optical and Quantum Electronics*, 2021, 53(2): 1–10.

[30] T. S. Mostafa, N. A. Mohammed, and E. S. M. El-Rabaie, "Ultracompact ultrafast-switching-speed all-optical 4 × 2 encoder based on photonic crystal," *Journal of Computational Electronics*, 2019, 18: 279–292.

[31] R. V. Nair and R. Vijaya, "Photonic crystal sensors: An overview," *Progress in Quantum Electronics*, 2010, 34(3): 89–134.

[32] N. Ayyanar, K. V. Sreekanth, G. T. Raja, and M. S. M. Rajan, "Photonic crystal fiber-based reconfigurable biosensor using phase change material," *IEEE Transactions on Nanobioscience*, 2021, 20(3): 338–344.

[33] S. A. Mitu, K. Ahmed, H. Abdullah, B. K. Paul, F. A. Al-Zahrani, S. K. Patel, *et al.,* "Exploring the optical properties of exposed-core-based photonic-crystal fibers," *Journal of Computational Electronics*, 2021, 20(3): 1260–1269.

[34] R. Kanmani, K. Ahmed, S. Roy, F. Ahmed, B. K. Paul, and M. S. M. Rajan, "The performance of hosting and core materials for slotted core Q-PCF in terahertz spectrum," *Optik*, 2019, 194: 163084.

[35] M. Danaie and B. Kiani, "Design of a label-free photonic crystal refractive index sensor for biomedical applications," *Photonics and Nanostructures-Fundamentals and Applications*, 2018, 31: 89–98.

[36] A. Habib, A. Rashed, H. M. El-Hageen, and A. M.

Alatwi, "Extremely sensitive photonic crystal fiber-based cancer cell detector in the terahertz regime," *Plasmonics*, 2021, 16(4): 1297–1306.

[37] S. A. Taya, "P-polarized surface waves in a slab waveguide with left-handed material for sensing applications," *Journal of Magnetism and Magnetic Materials*, 2015, 377: 281–285.

[38] S. A. Taya, "Ternary photonic crystal with left-handed material layer for refractometric application," *Opto-Electronics Review*, 2018, 26(3): 236–241.

[39] V. Devika and M. S. M. Rajan, "Hexagonal PCF of honeycomb lattice with high birefringence and high nonlinearity," *International Journal of Modern Physics B*, 2020, 34(10): 2050094.

[40] S. Singh, A. Upadhyay, D. Sharma, and S. A. Taya, "A comprehensive study of large negative dispersion and highly nonlinear perforated core PCF: theoretical insight," *Physica Scripta*, 2022, 97(6): 65504.

[41] J. N. Dash and R. Jha, "Graphene-based birefringent photonic crystal fiber sensor using surface plasmon resonance," *IEEE Photonics Technology Letters*, 2014, 26(11): 1092–1095.

[42] M. E. Rahaman, R. H. Jibon, H. S. Mondal, M. B. Hossain, A. A. M. Bulbul, and R. Saha, "Design and optimization of a PCF-based chemical sensor in THz regime," *Sensing and Bio-Sensing Research*, 2021, 32: 100422.

[43] Q. Liu, S. Li, and H. Chen, "Enhanced sensitivity of temperature sensor by a PCF with a defect core based on Sagnac interferometer," *Sensors and Actuators B: Chemical*, 2018, 254: 636–641.

[44] D. Chen, G. Hu, and L. Chen, "Dual-core photonic crystal fiber for hydrostatic pressure sensing," *IEEE Photonics Technology Letters*, 2011, 23(24): 1851–1853.

[45] D. Vigneswaran, N. Ayyanar, M. Sharma, M. Sumathi, M. Rajan, and K. Porsezian, "Salinity sensor using photonic crystal fiber," *Sensors and Actuators A: Physical*, 2018, 269: 22–28.

[46] M. Hossain and E. Podder, "Design and investigation of PCF-based blood components sensor in terahertz regime," *Applied Physics A*, 2019, 125: 1–8.

[47] A. Upadhyay, S. Singh, D. Sharma, and S. A. Taya, "A highly birefringent bend-insensitive porous core PCF for endlessly single-mode operation in THz regime: an analysis with core porosity," *Applied Nanoscience*, 2021, 11: 1021–1030.

[48] J. F. O'Hara, S. Ekin, W. Choi, and I. Song, "A perspective on terahertz next-generation wireless communications," *Technologies*, 2019, 7(2): 43.

[49] H. Thenmozhi, M. M. Rajan, V. Devika, D. Vigneswaran, and N. Ayyanar, "D-glucose sensor using photonic crystal fiber," *Optik*, 2017, 145: 489–494.

[50] A. Shafkat, A. N. Z. Rashed, H. M. El-Hageen, and A. M. Alatwi, "Design and analysis of a single elliptical channel photonic crystal fiber sensor for potential malaria detection," *Journal of Sol-Gel Science and Technology*, 2021, 98(1): 202–211.

[51] M. Islam, M. R. Islam, A. M. Al Naser, F. Anzum, and F. Z. Jaba, "Square structured photonic crystal fiber based THz sensor design for human body protein detection," *Journal of Computational Electronics*, 2021, 20: 377–386.

[52] M. Eid, A. N. Z. Rashed, A. A. M. Bulbul, and E. Podder, "Mono-rectangular core photonic crystal fiber (MRC-PCF) for skin and blood cancer detection," *Plasmonics*, 2021, 16: 717–727.

[53] A. A. M. Bulbul, H. Rahaman, S. Biswas, M. B. Hossain, and A. A. Nahid, "Design and numerical analysis of a PCF-based bio-sensor for breast cancer cell detection in the thz regime," *Sensing and Bio-Sensing Research*, 2020, 30: 100388.

[54] A. Upadhyay, S. Singh, D. Sharma, and S. A. Taya, "Analysis of proposed PCF with square air hole for revolutionary high birefringence and nonlinearity," *Photonics and Nanostructures-Fundamentals Applications*, 2021, 43: 100896.

[55] A. Upadhyay, S. Singh, D. Sharma, and S. A. Taya, "An ultra-high birefringent and nonlinear decahedron photonic crystal fiber employing molybdenum disulphide (MoS_2): a numerical analysis," *Material Science and Engineering B*, 2021, 270: 115236.

[56] N. A. Mohammed, O. E. Khedr, E. S. M. El-Rabaie, and A. A. M. Khalaf, "Literature review: on-chip photonic crystals and photonic crystal fiber for biosensing and some novel trends," *IEEE Access*, 2022, 10: 47419–47436.

[57] W. H. Organization, "Global tuberculosis report 2021," *World Health Organization*, 2021.

[58] M. S. Islam, J. Sultana, A. Dinovitser, B. Ng, and D. Abbott, "A novel zeonex based oligoporous-core photonic crystal fiber for polarization preserving terahertz applications," *Optics Communications*, 2018, 413: 242–248.

[59] A. A. M, Bulbul, F. Imam, M. Awal, and M. A. Mahmud, "A novel ultra-low loss rectangle-based porous-core PCF for efficient THz waveguidance: design and numerical analysis," *Sensors*, 2020, 20: 6500.

[60] H. El Hamzaoui, Y. Ouerdane, L. Bigot, G. Bouwmans, B. Capoen, A. Boukenter, *et al.*, "Sol-gel derived ionic copper-doped microstructured optical fiber: a potential selective ultraviolet radiation dosimete," *Optics Express*, 2012, 20(28): 29751–29760.

[61] S. Atakaramians, S. Afshar, H. Ebendorff-Heidepriem, M. Nagel, B. M. Fischer, D. Abbott, *et al.*, "THz porous fibers: design, fabrication and experimental characterization," *Optics Express*, 2009,

17(16): 14053–14062.

[62] I. Ishida, T. Akamatsu, Z. Wang, Y. Sasaki, K. Takenaga, and S. Matsuo, "Possibility of stack and draw process as fabrication technology for multi-core fiber," in *Optical Fiber Communication Conference*, United States, 2013, pp. 1–3.

[63] Y. Luo, J. Canning, J. Zhang, and G. D. Peng, "Toward optical fibre fabrication using 3D printing technology," *Optical Fiber Technology*, 2020, 58: 102299.

[64] M. L. Shofner, F. J. Rodríguez-Macías, R. Vaidyanathan, and E. V. Barrera, "Single wall nanotube and vapor grown carbon fiber reinforced polymers processed by extrusion freeform fabrication," *Composites: Part A*, 2003, 34: 1207–1217.

[65] A. M. Cubillas, S. Unterkofler, T. G. Euser, B. J. M. Etzold, A. C. Jones, P. J. Sadler, *et al.*, "Photonic crystal fibres for chemical sensing and photochemistry," *Chemical Society Reviews*, 2013, 42(22): 8629–8248.

[66] E. J. F. Dickinson, H. Ekström, and E. Fontes, "COMSOL Multiphysics®: finite element software for electrochemical analysis. A mini-review," *Electrochemical Communications*, 2014, 40: 71–74.

[67] A. A. M. Bulbul, R. H. Jibon, S. Biswas, S. T. Pasha, and M. A. Sayeed, "Photonic crystal fiber-based blood components detection in THz regime: design and simulation," *Sensors International*, 2021, 2: 100081.

[68] M. S. Islam, J. Sultana, K. Ahmed, M. R. Islam, A. Dinovitser, B. W. H. Ng, *et al.*, "A novel approach for spectroscopic chemical identification using photonic crystal fiber in the terahertz regime," *IEEE Sensors Journal*, 2017, 18(2): 575–582.

[69] N. R. Ramanujam, S. K. Patel, N. M. Reddy, S. A. Taya, D. Vigneswaran, and M. S. M. Rajan, "One-dimensional ring mirror-defect photonic crystal for detection of mycobacterium tuberculosis bacteria," *Optik*, 2020, 219: 165097.

[70] A. H. Aly, D. Mohamed, Z. A. Zaky, Z. S. Matar, N. S. Abd El-Gawaad, A. S. Shalaby, *et al.*, "Novel biosensor detection of tuberculosis based on photonic band gap materials," *Materials Research*, 2021, 24(3).

[71] S. A. Taya, M. G. Daher, I. Colak, and O. M. Ramahi, "Highly sensitive nano-sensor based on a binary photonic crystal for the detection of mycobacterium tuberculosis bacteria," *Journal of Materials Science: Materials in Electronics*, 2021, 32: 28406–28416.

[72] M. S. Mohamed, M. F. O. Hameed, N. F. F. Areed, M. M. El-Okr, and S. S. A. Obayya, "Analysis of highly sensitive photonic crystal biosensor for glucose monitoring," *The Applied Computational Electromagnetics Society Journal(ACES)*, 2016, 836–842.

[73] K. Ahmed, M. I. Islam, B. K. Paul, M. S. Islam, S. Sen, S. Chowdhury, *et al.*, "Effect of photonic crystal fiber background materials in sensing and communication applications," *Materials Discovery*, 2017, 7: 8–14.

[74] N. A. Mohammed, M. M. Hamed, A. A. M. Khalaf, and S. EL-Rabaie, "Malaria biosensors with ultra-sensitivity and quality factor based on cavity photonic crystal designs," *The European Physical Journal Plus*, 2020, 135(11): 933.

[75] N. A. Mohammed, M. M. Hamed, A. A. M. Khalaf, A. Alsayyari, and S. El-Rabaie, "High-sensitivity ultra-quality factor and remarkable compact blood components biomedical sensor based on nanocavity coupled photonic crystal," *Results in Physics*, 2019, 14: 102478.

[76] S. K. Srivastava, C. J. M. Van Rijn, and M. A. Jongsma, "Biosensor-based detection of tuberculosis," *RSC Advances*, 2016, 6(22): 17759–17771.

[77] F. A. Al-Zamel, "Detection and diagnosis of Mycobacterium tuberculosis," *Expert Review of Anti Infective Therapy*, 2009, 7(9): 1099–1108.

[78] S. Gull and S. Akbar, "Artificial intelligence in brain tumor detection through MRI scans, advancements and challenges," *Artificial Intelligence and Internet of Things*, 2021: 241–276.

[79] A. H. Yassin, A. A. A. Nasser, R. AbdelRasoul, and O. E. Khedr, "Neural based prediction of scattering and noise parameters for solid state microwave transistors," in *2014 31st National Radio Science Conference(NRSC), IEEE*, Egypt, 2014, pp. 281–287.

[80] E. H. Thomas, "Tuberculosis (TB) workup," *Medscape*, 2022.

[81] K. G. Castro, Goldberg, J. A. Jereb, P. LoBue, G. H. Mazurek, and A. Vernon, "Updated guidelines for using interferon gamma release assays to detect Mycobacterium tuberculosis infection-United States, 2010," *Recommendations and Reports*, 2010, 59: 1–25.

[82] M. Kruse and W. Cruikshank, "End TB strategy: time to move on from the skin test to the interferon-γ release assays," *American Journal of Public Health*, 2019, 109(8): 1102–1104.

[83] W. H. Organization, "Chest radiography in tuberculosis detection: summary of current WHO recommendations and guidance on programmatic approaches," *World Health Organization*, 2016.

[84] B. Datta, A. K. Prakash, D. Ford, P. K. Tanwar, P. Goyal, P. Chatterjee, *et al.*, "Comparison of clinical and cost-effectiveness of two strategies using mobile digital x-ray to detect pulmonary tuberculosis in rural India," *BMC Public Health*, 2019, 19(99): 1–8.

[85] A. E. Nijhawan, P. A. Iroh, L. S. Brown, D. Winetsky, and E. Porsa, "Cost analysis of tuberculin skin test and the QuantiFERON-TB gold in-tube test for tuberculosis screening in a correctional setting in

Dallas, Texas, USA," *BMC Infectious Diseases*, 2016, 16(564): 1–11.

[86] N. Ayyanar, G. T. Raja, M. Sharma, and D. S. Kumar, "Photonic crystal fiber-based refractive index sensor for early detection of cancer," *IEEE Sensors Journal*, 2018, 18(17): 7093–7399.

[87] K. Ahmed, F. Ahmed, S. Roy, B. K. Paul, M. N. Aktar, D. Vigneswaran, *et al.*, "Refractive index-based blood components sensing in terahertz spectrum," *IEEE Sensors Journal*, 2019, 19(9): 3368–3375.

[88] A. Kumar, P. Verma, and P. Jindal, "Decagonal solid core PCF based refractive index sensor for blood cells detection in terahertz regime," *Optical and Quantum Electronics*, 2021, 53(165): 1–13.

[89] S. Sen, M. Abdullah-Al-Shafi, and M. A. Kabir, "Hexagonal photonic crystal fiber (H-PCF) based optical sensor with high relative sensitivity and low confinement loss for terahertz (THz) regime," *Sensing and Bio-Sensing Research*, 2020, 30: 100377.

[90] M. S. Hossain, M. M. Kamruzzaman, S. Sen, M. M. Azad, and M. S. H. Mollah, "Hexahedron core with sensor based photonic crystal fiber: An approach of design and performance analysis," *Sensing and Bio-Sensing Research*, 2021, 32: 100426.

[91] B. K. Paul, M. Haque, K. Ahmed, and S. Sen, "A novel hexahedron photonic crystal fiber in terahertz propagation: design and analysis," *Photonics*, 2019, 6(1): 32.

[92] N. Suhaimi, I. K. Yakasai, E. Abas, S. Kaijage, and F. Begum, "Modelling and simulation of novel liquid-infiltrated PCF biosensor in Terahertz frequencies," *IET Optoelectronics*, 2020, 14: 411–416.

[93] A. A. M. Bulbul, R. H. Jibon, S. K. Das, T. Roy, A. Saha, and M. B. Hossain, "PCF based formalin detection by exploring the optical properties in THz regime," *Nanoscience & Nanotechnology-Asia*, 2021, 11: 314–321.

[94] V. S. Chaudhary and D. Kumar, "TOPAS based porous core photonic crystal fiber for terahertz chemical sensor," *Optik*, 2020, 223: 165562.

[95] V. Kaur and S. Singh, "Design approach of solid-core photonic crystal fiber sensor with sensing ring for blood component detection," *Journal of Nanophotonics*, 2019, 13: 26011.

[96] M.S. Islam, J. Sultana, A. Dinovitser, K. Ahmed, B. W. H. Ng, and D. Abbott, "Sensing of toxic chemicals using polarized photonic crystal fiber in the terahertz regime," *Optics Communications*, 2018, 426: 341–347.